



# Investigation on high-velocity impact of micron particles using material point method



Ping Liu <sup>a</sup>, Yan Liu <sup>a,b,\*</sup>, Xiong Zhang <sup>a</sup>, Yu Guan <sup>c</sup>

<sup>a</sup> School of Aerospace Engineering, Tsinghua University, Beijing 100084, China

<sup>b</sup> State Key Laboratory of Explosion Science and Technology, Beijing Institute of Technology, Beijing 100081, China

<sup>c</sup> Beijing Institute of Electronic System Engineering, Beijing 100854, China

## ARTICLE INFO

### Article history:

Received 4 October 2013  
 Received in revised form  
 24 June 2014  
 Accepted 3 September 2014  
 Available online 16 September 2014

### Keywords:

High-velocity impact  
 Space debris  
 Material point method  
 Crater morphology mode

## ABSTRACT

Continuous high-velocity impact of micro space debris and micro-meteoroids may cause significant accumulative damages to spacecrafts. The process of high-velocity impact of micron aluminum particles on the aluminum target is investigated with the material point method (MPM). As a meshfree particle method, MPM is very suitable for solving high-velocity impact problems owing to its prominent advantages of dealing with fracture, fragmentation and moving material interface over the traditional mesh-based methods. The target plate is modeled as semi-infinite media since its thickness is much larger than the characteristic length of the projectile particles. The micron particles are projected to the target individually and in group with different angles and different velocities. The predicted impact responses and dimensions of the craters agree well with the experimental results and the empirical equations. The influences of the flux density, the projectile angle and the impact velocity are thoroughly investigated, and the morphology modes of the crater group are concluded. Finally, an empirical formula is proposed for the crater depth under impact of particle group.

© 2014 Elsevier Ltd. All rights reserved.

## 1. Introduction

Natural meteoroids and man-made space debris particles are threatening the safety of near-earth orbiters. Every spacecraft in orbit is exposed to a certain flux of impacting particles, especially the millimeter-sized or micron particles. The impact risks need be assessed and shielding measures must be taken to avoid the failure or the decrease in performances of the space vehicles. Even after short exposure to the space environment, the surfaces will be covered with impacts from small-sized debris. The knowledge on impact from micron particles can be obtained through dedicated *in situ* experiments or through the analysis of the crafts returned from space, e.g. satellites or parts thereof [1,2]. Till now, the experiments of high-velocity impact need specially strict conditions and advanced equipments, which may cost a large amount of money and time. What's more, the situations in low earth orbit cannot be exactly reproduced or even the desired velocity conditions cannot be reached, not to mention that it is difficult to obtain and analyze

the experimental data. Computational simulations are necessary ways to investigate the processes of high-velocity impact of materials.

In high-velocity impact, the magnitude of the stress wave is usually much larger than the strength of the projectile and the target, which makes extremely large local deformation and local failure of the material. This characteristic of high-velocity impact process brings many challenges to computational methods.

In the early stage of high-velocity impact research, Lagrangian or Eulerian mesh-based method were popular [3]. In Lagrangian mesh-based method, large deformation will lead to element distortion [4], which result in sharp decrease in time step size and the computation will abnormally terminate if the volume becomes very close to zero and even negative [5]. Eulerian mesh-based method, on the other hand, has the difficulty in tracking history variables and material interfaces [6]. Arbitrary Lagrangian–Eulerian method (ALE) combined the ideas from both the methods to overcome the above disadvantages [7], but the treatment of complex 3D problems is still under investigation. Since mid 1990s, meshfree particle methods (also called as meshless methods) have been paid much attention to and have shown successful applications in problems involving in large deformation. Typical meshfree particle methods include smoothed particle hydrodynamics (SPH)

\* Corresponding author. School of Aerospace Engineering, Tsinghua University, Beijing 100084, China. Tel.: +86 10 62789122.

E-mail addresses: [yan-liu@tsinghua.edu.cn](mailto:yan-liu@tsinghua.edu.cn) (Y. Liu), [xzhang@tsinghua.edu.cn](mailto:xzhang@tsinghua.edu.cn) (X. Zhang).

method [8], element free Galerkin method [9], reproducing kernel particle method [10], material point method (MPM) [11], radial basis function collocation method [12,13], meshless weighted least-square method [14], and general particle algorithm method [15].

MPM was proposed by Sulsky et al. [11] as an extension of particle-in-cell method to solid mechanics. One set of Lagrangian points and one Eulerian background grid are used for discretization in MPM, as shown in Fig. 1. Lagrangian points carry all the physical variables, such as the mass, the density, the velocity, the stress, the strain, which can describe the deformation and the boundary of the material. The usage of Lagrangian points avoids the difficulties in Eulerian method that the history variables are not easy to be traced and the problems caused by convection terms. Eulerian background grid is used to solve momentum equations and to calculate spatial derivatives, which overcomes the shortcomings in Lagrangian method that large deformation causes element distortion. As the result, MPM owns the advantages of both Lagrangian and Eulerian methods but overcomes their difficulties, and can solve problems involving in extremely large deformation. In each step, the traced variables of Lagrangian points are mapped onto the Eulerian grid nodes. Then the momentum equations are solved on grid nodes, and the particle variables are updated by mapping variable increments back onto the points. Finally the deformed grid is abandoned. Different with other meshfree particle methods, the critical time step size in MPM is controlled by the element size of the background grid instead of the characteristic length between points. So a time step size close to the initial time step size can be used throughout the simulation, even when very large deformation happens. What's more, no neighbor point search is needed in MPM. MPM ensures single-valued velocity field automatically even if no specific contact algorithm is adopted, and very efficient contact algorithm [16] based on the usage of the grid can also be adopted in MPM. Compared with the other meshfree methods, MPM is a very efficient and stable method for simulating high-velocity impact problems [17].

Owing to the above advantages, MPM has been developed fast and applied in many areas. MPM can effectively solve the problems of extremely large deformation and moving discontinuities, such as impact problems [18], granular flow [19], explosion [20], dynamic fracture [21,22], fluid-structure interaction [23], and multiscale analysis [24]. MPM was firstly applied in impact problems by analyzing Taylor bar problems [18,25]. Ma et al. [26] studied the penetration into thin and thick targets under hyper-velocity impact with MPM. Huang et al. [27] analyzed the influences of the grid size and the particle size on the results of the high-velocity impact simulation. They obtained the debris cloud morphologies in good agreement with the experimental results. Liu et al. [24] proposed a multiscale framework for high-velocity impact process, which combined molecular dynamics (MD) and MPM. MD was used to determine equation of state (EOS) parameters from micro level. The parameters are then transferred to MPM to simulate the high-velocity impact process. Hugoniot curves and debris cloud shapes

obtained with the multiscale framework agreed well with the experimental results. They proposed an empirical formula for the percentage of phase change material in high-velocity impact process based on a large number of simulations. Gong et al. [28] reproduced the micro-structure model of aluminium foam from CT images, and studied different Whipple shielding structures under high-velocity impact directly based on the MPM micro-structure model. Numerical results can predict well the damage and the holes on the shielding structure.

In this paper, the high-velocity impacts of micron particles are modeled and investigated with MPM. The main contribution of the paper is that the shape and the pattern of the craters caused by impact are thoroughly investigated and concluded, and the effects of the impact angle and the impact velocity are obtained. The result of particle group impact is firstly investigated with MPM, and an empirical equation is also proposed. The formulae of MPM are introduced in Section 2 focusing on the application in high-velocity impact process. The impact of single micron particle is simulated in Section 3, and the influences of different angles and velocities are studied. The impact of particle group is simulated in Section 4. The crater morphology is studied and categorized with different impact velocities and angles. The non-dimensional scaling analysis is carried out to derive the empirical formulae. The paper is concluded in Section 5.

## 2. Material point method and the material model

Discretized equations in MPM can be derived in updated Lagrangian formulation from the following governing equations on the current configuration.

$$\sigma_{ij,j} + \rho b_i = \rho \ddot{u}_i, \quad \text{in } \Omega \quad (1)$$

with the boundary conditions

$$u_i = \bar{u}_i, \quad \text{on } \Gamma_u \quad (2)$$

$$\sigma_{ij} n_j = \bar{t}_i, \quad \text{on } \Gamma_t \quad (3)$$

where  $i, j = 1, 2, 3$  are spatial coordinate indices and Einstein summation convention is invoked.  $\rho$  and  $\rho_0$  are the current and the initial material density, respectively.  $\rho J = \rho_0$ , where  $J$  is the determinant of the deformation gradient tensor  $F_{ij} = \partial x_i / \partial X_j$ . The superposed dot represents the derivative with respect to time, and “,” is the spatial derivative.  $b_i$  is the body force per unit mass.  $\bar{t}_i$  is the boundary surface traction.  $u_i$  is the displacement vector, and  $\sigma_{ij}$  is the Cauchy stress tensor.  $\Gamma_t$  and  $\Gamma_u$  represent the traction boundary and the displacement boundary, respectively.  $n_i$  is the unit outward normal vector of the boundary. The Cauchy stress can be decomposed as

$$\sigma_{ij} = -p \delta_{ij} + s_{ij} \quad (4)$$

where  $s_{ij}$  is the deviatoric stress component,  $p = -\sigma_{ii}$  represents the pressure, and  $\delta_{ij}$  is Kronecker delta symbol.

Inside each MPM step, the regular Eulerian background grid is binded to the Lagrangian points and deforms with the Lagrangian points in the same way. Any variables on the Lagrangian point can be interpolated from the grid.

$$f_p = f(\mathbf{x}_p, t) = \sum_{l=1}^{n_g} N_l(\mathbf{x}_p) f_l(t) = \sum_{l=1}^{n_g} N_{lp} f_l \quad (5)$$

where the subscript  $l$  indicates the Eulerian grid node number, and the subscript  $p$  denotes the Lagrangian point number.  $N_{lp} = N_l(\mathbf{x}_p)$

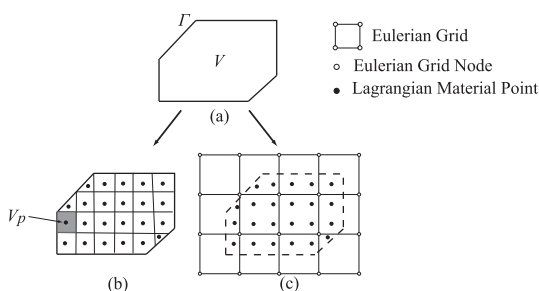


Fig. 1. Schematic diagram of discretization in MPM.

can be the standard finite element (FE) shape function.  $n_g$  is the number of grid node associated with the material point. The time derivative and the spatial derivative of any field variable can be calculated respectively by differentiating the nodal variable and the shape functions, as what is done in standard FEM. The density of an arbitrary point is approximated in MPM by

$$\rho(\mathbf{x}) = \sum_{p=1}^{n_p} m_p \delta(\mathbf{x} - \mathbf{x}_p) \quad (6)$$

where  $n_p$  is the number of Lagrangian points.  $\delta(\mathbf{x})$  is the Dirac  $\delta$  function.

Substituting equations (5) and (6) into the weak-form.

$$\int_V \delta v_{i,j} \sigma_{ij} dV + \int_V \delta v_i \rho \ddot{u}_i dV - \int_V \delta v_i \rho b_i dV - \int_{\Gamma_i} \delta v_i \bar{t}_i d\Gamma = 0 \quad (7)$$

of the governing equation (1) leads to

$$f_{ii}^{kin} = f_{ii}^{ext} + f_{ii}^{int} \quad (8)$$

where  $\delta v_i$  is the virtual velocity, and  $\delta v_i = 0$  on  $\Gamma_u$ . It should be noted the arbitrariness of nodal virtual velocities  $\delta v_{il}$  is invoked in deriving equation (8).

The inertial force.

$$f_{ii}^{kin} = \sum_{j=1}^{n_g} M_{ij} \ddot{u}_{ij}, \quad (9)$$

the external force

$$f_{ii}^{ext} = \sum_{p=1}^{n_p} m_p N_{ip} b_{ip} + \sum_{p=1}^{n_p} N_{ip} \bar{t}_{ip} h^{-1} \frac{m_p}{\rho_p}, \quad (10)$$

where  $h$  is the thickness of a very thin layer of the traction boundary to apply the traction boundary condition, and the internal force

$$f_{ii}^{int} = - \sum_{p=1}^{n_p} N_{ip,j} \sigma_{ijp} \frac{m_p}{\rho_p}. \quad (11)$$

The mass matrix element  $M_{ij} = \sum_{p=1}^{n_p} N_{ip} N_{jp} m_p$ . The lumped mass matrix  $M_{ii} = \sum_{j=1}^{n_g} M_{ij} = \sum_{p=1}^{n_p} N_{ip} m_p$  is usually adopted to obtain explicit time integration, and the inertial force is written in the following form in explicit integration.

$$f_{ii}^{kin} = M_{ii} \ddot{u}_{ii} = \dot{p}_{ii} \quad (12)$$

where  $p_{ii}$  is the momentum of the grid node. The strain rate of the Lagrangian point can be calculated by nodal velocities as

$$\dot{\epsilon}_{ijp} = \frac{1}{2} (v_{ip,j} + v_{jp,i}) = \frac{1}{2} \left( \sum_{l=1}^{n_g} N_{lp,j} v_{il} + \sum_{l=1}^{n_g} N_{lp,i} v_{jl} \right) \quad (13)$$

If the variables on and before the time level  $t^k$  are known, the flowchart of one MPM step updating variables from  $t^k$  to  $t^{k+1}$  is as follows.

1. A regular Eulerian background grid is used, and the masses and the momenta of material points are mapped to the new background grid nodes.

2. The essential boundary conditions are imposed on the grid nodes. If the boundary is fixed in  $i$ -th direction, then  $p_{ii}^{k-\frac{1}{2}} = 0$ .
3. The velocity of the Eulerian grid nodes, and then the increments of the strain tensor and the vorticity tensor of the material points are calculated. The density of the material point is also updated with the strain increment. After that, the new stress  $\sigma_{ijp}^k$  can be obtained by invoking the constitutive model.
4. The internal and external forces can be obtained from equations (10) and (11). If the boundary is fixed in  $i$ -th direction, then  $f_{ii}^k$  should be set to zero.
5. The momenta of grid nodes are updated by integrating equation (12).
6. The velocities of the material points are updated using interpolation of the nodal accelerations, and the positions of the material points are updated using interpolation of the nodal velocities.
7. The deformed grid is abandoned and the initial regular background grid will be used in the next step.

The readers can refer to literature [11,25,29] for discretization and application details of material point method. In the above procedure, the stress is updated at the beginning of each step, which is called update stress first (USF) scheme. Also, updating the stress at the end of each step can be used, and the corresponding two kinds of schemes are called update stress last (USL) and modified update stress last (MUSL). Ref. [29] discussed the details of different schemes.

The transmitting boundary condition, also called as non-reflecting or silent boundary condition, is used for simulating infinite and semi-infinite media with finite domain. Its basic idea originated from using the viscous damping forces to absorb the reflecting wave on the boundary of finite domain [30] and was recently introduced to material point method by Shen and Chen [31]. Effective boundary traction is applied in the transmitting boundary condition to reduce the reflection when the stress wave reaches the boundary. The boundary traction vector  $\bar{\mathbf{t}}$  on the transmitting boundary in MPM is calculated as.

$$\bar{\mathbf{t}}_{nor} = -\rho c_d \mathbf{v}_{nor} \quad (14)$$

$$\bar{\mathbf{t}}_{tan} = -\rho c_s \mathbf{v}_{tan} \quad (15)$$

where  $\bar{\mathbf{t}}_{nor}$  and  $\bar{\mathbf{t}}_{tan}$  are the normal component and the tangential component of  $\bar{\mathbf{t}}$ .  $c_d$  and  $c_s$  are the dilatational wave speed and the shear wave speed, respectively.  $\mathbf{v}_{nor}$  and  $\mathbf{v}_{tan}$  are the normal component and the tangential component of the grid node velocity. The traction (14) and (15) is added to the external nodal force through the second right-hand-sided term in equation (10).

In standard MPM, the velocities of the material points are determined by the single-valued field of the Eulerian grid, which can guarantee that different objects do not penetrate each other. In other words, a non-slip contact constraint is inherent in standard MPM. The friction between different objects in standard MPM is taken into consideration in a sticky way. An appropriate contact algorithm should be employed in the low-velocity impact problems to ensure good description of the contact process to obtain high accuracy. But for high-velocity impact problems, though the non-slip contact condition does not precisely describe the true contact process during impact, the numerical accuracy of standard MPM can still be very good since the contact pressure is extremely large and the contact friction is mainly sticky friction.

The Johnson–Cook strength model with a failure model and the Mie–Grüneisen equation of state (EOS) are employed in this paper.

The strength model is for updating the deviatoric stress  $s_{ij}$ , and the EOS is used to update the pressure  $p$ . The yield stress  $\sigma_y$  is expressed as the function of the effective plastic strain  $\epsilon^p$ , the strain rate  $\dot{\epsilon}$ , and the temperature  $T$  in Johnson–Cook model [32],

$$\sigma_y = (A + B\epsilon^{pn})(1 + C\ln\dot{\epsilon}^*) (1 - T^{*m}) \quad (16)$$

where  $A, B, n, c, m$  are material parameters which can be determined by experiments.  $\dot{\epsilon}^* = \dot{\epsilon}/\dot{\epsilon}_0$  is the dimensionless equivalent strain rate, and the reference strain rate  $\dot{\epsilon}_0 = 1.0s^{-1}$ .  $T^* = (T - T_{room}) / (T_{melt} - T_{room})$  is the dimensionless temperature, where  $T_{room}$  and  $T_{melt}$  are the room temperature and the melting temperature, respectively. A sophisticated failure model [33] was developed for the Johnson–Cook model. The equivalent failure strain in the failure model can be calculated as

$$\epsilon_f^p = [D_1 + D_2 \exp D_3 \sigma^*] [1 + D_4 \ln \dot{\epsilon}^*] [1 + D_5 T^{*m}] \quad (17)$$

where  $D_1, D_2, D_3, D_4, D_5$  are material constants.  $\sigma^* = \sigma_m / \bar{\sigma}$  is the stress triaxiality, where  $\sigma_m$  is the mean stress and  $\bar{\sigma}$  is the von Mises effective stress. The damage is calculated by

$$D = \sum \frac{\Delta \epsilon^p}{\epsilon_f^p} \quad (18)$$

where  $\Delta \epsilon^p$  is the increment of effective plastic strain in each step. When the damage of one material point reaches unity, the point will fail. Failure points cannot sustain the deviatoric stress  $s_{ij}$  and the tensile stress.

The pressure in high-velocity impact is calculated by Mie–Grüneisen EOS.

$$p = p_H \left(1 - \frac{\gamma \mu}{2}\right) + \gamma_0 E_0 \quad (19)$$

where  $\gamma$  is the Mie–Grüneisen parameter, which satisfies  $\gamma_0 \rho_0 = \gamma \rho$ .  $\mu = \rho / \rho_0 - 1$ , and  $E_0$  is the initial specific internal energy.  $p_H$  is the pressure on the Hugoniot curve,

$$p_H = \begin{cases} \frac{\rho_0 c_0 \mu (1 + \mu)}{[1 - (s - 1)\mu]^2} & \text{for } \mu \geq 0 \\ \rho_0 c_0 \mu & \text{for } \mu < 0 \end{cases} \quad (20)$$

where  $c_0$  is the sound speed and  $s$  is a material constant.

Phase change may happen during high-velocity impact process. The influence of phase change depends greatly on the impact velocity. Lee et al. [34] experimentally studied the impact on aluminum plate. They found that the plastic flow is a very important influential factor on excavation and the melting material is very little when the impact velocity is below 5 km/s. While the impact velocity above 8 km/s will bring obvious melting process. Wingate et al. [35] also employed Mie–Grüneisen EOS for the simulation of hyper-velocity micro-particle impact of single crystal aluminum when they investigated the performances of different numerical methods. They found that the numerical results of impact velocity below 14 km/s are reliable in comparison with experimental results. All of the impact velocities investigated in the current paper are below 5 km/s, and most of the impact velocities are even below 2.3 km/s. Employment of Mie–Grüneisen EOS, therefore, should be reasonable though the influence of phase change is neglected in Mie–Grüneisen EOS.

### 3. High-velocity impact of single micron particle

#### 3.1. Problem setup

Sphere debris is used throughout the simulation because previous researches pointed out that the influences of projectile shape in high-velocity impact is negligible [3]. The typical thickness of the front panel of the shielding plate of spacecrafts is in the order of millimeter, and the micron projectile is smaller in orders than the shielding plate. The impact of micron particles, therefore, can be modeled as impact on a very thick target, which implies that the target should be investigated as a semi-infinite domain.

Fig. 2 shows the normal impact of a single sphere on the semi-infinite target, and gives a local view of the definition of the crater dimensions. Experimental results suggested that the crater approaches to a hemisphere with velocity increasing [3].  $v_p$  is the impact velocity.  $D_c$  is the diameter of the crater surface.  $C_p$  is the crater depth, which is defined as the distance from the bottom center to the initial (undeformed) surface.

The schematic view of the oblique high-velocity impact is shown in Fig. 3, where  $v_s$  and  $v_n$  are the tangential (scraping) and the normal components of the impact velocity  $v_p$ , respectively. The impact angle  $\theta$  is defined as the angle between  $v_p$  and the surface normal. Same as normal impact, the crater depth  $C_p$  is defined as the distance from the bottom center to the initial position of the surface. The scraping impact energy in oblique impact makes the pithead of the crater change to an ellipse instead of a circle.  $D_{min}$  is the length of the minor axis of the pithead ellipse, and  $D_{max}$  is the length of the major axis.

Both the projectile and the target are made of aluminum alloy Al2024. The material properties for the Johnson–Cook model [32,33] and the Mie–Grüneisen EOS [36] are listed in Table 1.

The target is simulated as a block-shaped domain with the transmitting boundary condition applied to all the boundaries except the impacted surface. The transmitting boundary condition is used to reduce the reflection of the stress wave on the boundary and ensure that the major part of the stress wave can travel outside the domain, which is to model the semi-infinite media.

The diameter of the sphere projectile simulated here is 20  $\mu m$ . The normal impact and two oblique impacts of the angles 15° and 30° are simulated. The impact velocity  $v_p$  ranges from 700 m/s to 5000 m/s.

The convergence analysis of the grid spacing and the material point spacing is carried out to determine the appropriate discretization scale balancing the numerical accuracy and the computational burden. The details of four models with different discretizations for the case normal impact  $v_p = 2200$  m/s are listed in Table 2.  $h_p$  and  $h_e$  are the material point spacing and the element size of background grid, respectively.  $h_p^t$  denotes the spacing for the target, and  $h_p^p$  denotes the spacing for the projectile.  $h_p^p$  is smaller than  $h_p^t$  in models 1 to 3 in order to describe the shape of the

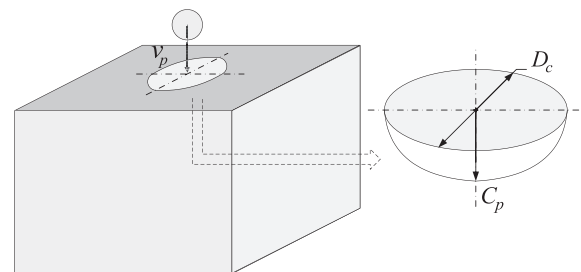


Fig. 2. Schematic diagram of the normal impact of a single sphere debris and the magnified view and dimensions of the crater.

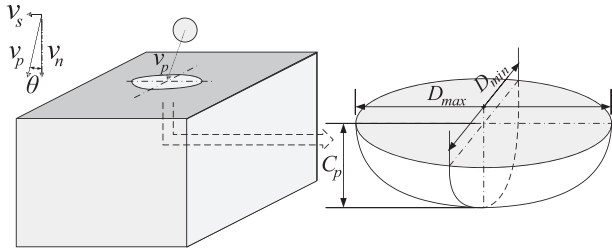


Fig. 3. Schematic diagram of the oblique impact of a single sphere debris and the magnified view and dimensions of the crater.

Table 1

Material properties of the projectile and the target.  $E$  and  $\nu$  are the Young's modulus and Poisson's ratio, respectively. The other material parameters were explained in Section 2.

Johnson–Cook strength model							
$\rho$ (g/cm <sup>2</sup> )	$C_p$ (J/(kg K))	$T_{melt}$ (K)	$A$ (MPa)	$B$ (MPa)	$n$	$C$	$m$
2.77	875	775	265	426	0.34	0.015	1.0
Johnson–Cook strength model							
$E$ (GPa)	$\nu$	$D_1$	$D_2$	$D_3$	$D_4$	$D_5$	
73	0.33	-0.77	1.45	-0.47	0.0	1.6	
Mie–Grüneisen EOS							
$c_0$ (m/s)			$s$				$\gamma_0$
5330			1.34				2.0

projectile more precisely.  $N_p$  is the number of material points, and  $N_e$  is the number of grid elements.  $E_i^r$  is the final internal energy of the whole system normalized by the initial kinetic energy, that is, the dimensionless residual internal energy.  $C_p$  is the crater depth.  $E_i^r$  and  $C_p$  respectively serve as a global indicator and a local indicator of the accuracy. Model 4 has the finest discretization, which is used as the comparison baseline. Obvious convergence can be observed in Table 2. The result differences between model 3 and 4 are very small though the number of grid nodes in model 3 is only one eighth of that in model 4. So the discretization model 3 (2,016,776 material points and 375,000 grid elements) is adopted for the simulation of impact of single particle.

To validate that the treatment of contact friction in a sticky way in standard MPM is appropriate in high-velocity impact problems, six simulations with a contact algorithm and the friction coefficient  $\mu_f$  from 0.05 to 0.9 are carried out for oblique impact and compared with standard MPM simulation. The impact velocity is 2200 m/s and the inclined angle is 30°. The final crater morphologies are shown in Fig. 4, where all the results, including the standard MPM results and the results with special contact friction algorithm, are very close. The validation example demonstrates that the inherent sticky friction in standard MPM is suitable for high-velocity impact simulation.

Table 2

The models with different discretization and the results for convergence analysis.

Model no.	$h_p^i$ (mm)	$h_p^p$ (mm)	$h_e$ (mm)	$N_p$	$N_e$	$E_i^r$	$C_p$ (mm)
1	0.002	0.001	0.004	252,112	47,500	0.9302	0.0143
2	0.0015	0.00075	0.003	601,701	113,900	0.9256	0.0162
3	0.001	0.0005	0.002	2,016,776	375,000	0.9295	0.0175
4	0.0005	0.0005	0.001	16,016,776	3,000,000	0.9193	0.0180

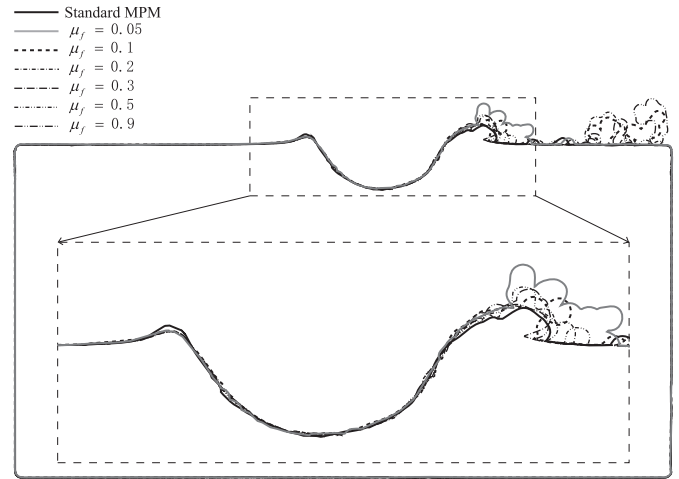


Fig. 4. Comparison of morphologies after impact calculated by standard MPM and MPM with different contact friction coefficients. The impact velocity is 2200 m/s and the inclined angle is 30°.

### 3.2. Empirical volume-energy formula for normal impact

The hemispherical theory states that when velocity increases, the crater shape factor  $C_p/D_c$  tends to 1/2 [3]. Another well-known theory, the isotropic uniform expansion theory [37,38], which evolves from the hemispherical theory, points out that the crater dimensions can be expressed as [39]

$$\frac{D_c}{d_p} = 2 \frac{C_p}{d_p} + 1.4 \left[ 1 - \left( \frac{\rho_p}{\rho_t} \right)^{\frac{2}{3}} \left( \frac{Y_p}{Y_t} \right)^{\frac{1}{3}} \right] \quad (21)$$

where  $\rho_p$  is the density of the projectile,  $Y_p$  is the strength of the projectile,  $\rho_t$  is the density of the target, and  $Y_t$  is the strength of the target.

As the projectile and the target are made of the same material,  $\rho_p/\rho_t=Y_p/Y_t=1$ , the isotropic uniform expansion theory degenerates to the hemispherical theory. The empirical 'volume-energy formula' can be obtained by fitting experimental results with the isotropic expansion theory as [37,38]

$$\frac{C_p}{d_p} = 0.27 \left( \sqrt{\frac{\rho_p}{Y_t}} v_p \right)^{\frac{2}{3}} \quad (22)$$

### 3.3. MPM results of normal high-velocity impact

One process of normal impact of single particle is shown in Fig. 5. The impact velocity is 2200 m/s. The projectile is shown with white color, and the effective stress contour is plotted for the target in the first line from (a) to (d), where the color map denotes the range from zero to 600 MPa. The pressure contour is demonstrated in the second line from (e) to (h), and the range of the color map is from -600 MPa to 600 MPa. The spreading of stress wave in radial direction can be clear seen. The projectile as well as the impacted area of the target is fragmented under such extreme pressure. Finally the crater is formed and the fragmented materials splash to the surface or even fly out of the computational region.

Fig. 6 demonstrates the simulation results of the crater shape factor  $C_p/D_c$  versus the impact velocity. The crater shape factor increases rapidly with the velocity, and finally reaches around 1/2, which agrees very well with experimental results [40]. In the

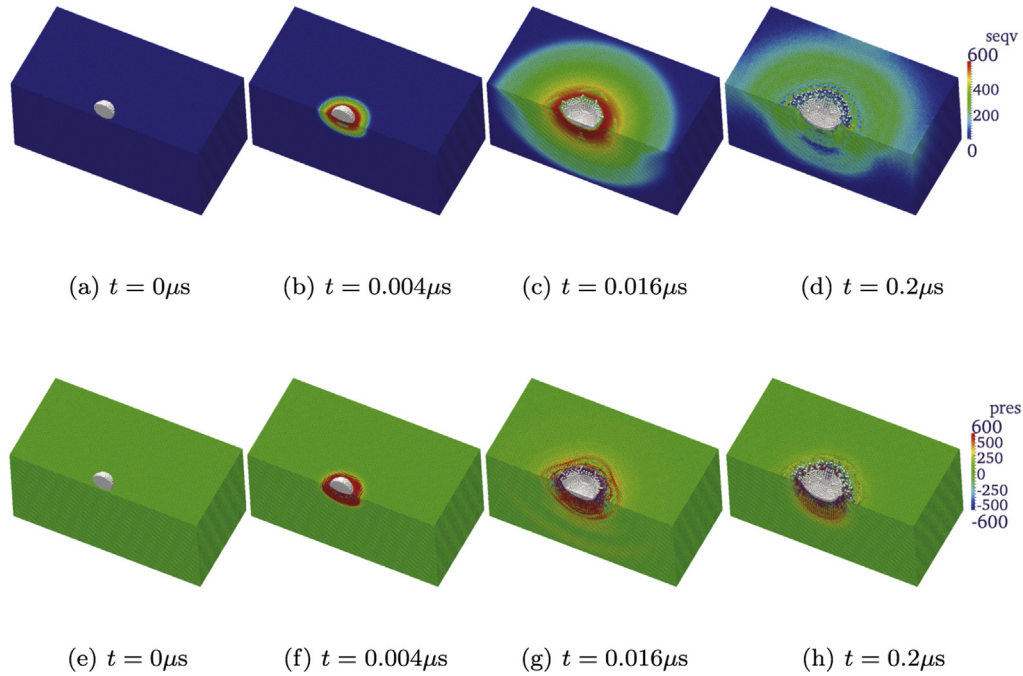


Fig. 5. Typical process of normal impact of single particle. The impact velocity is 2200 m/s.

experiments, the diameter of the sphere is 5 mm, and the same aluminum material is used for the projectile and the target. The impact velocity is up to 7350 m/s.

Fig. 7 shows the variation of the dimensionless crater depth  $C_p/d_p$  versus the impact velocity. The numerical results are generally consistent with the volume-energy formula, but smaller when the velocity is relative low. When the velocity is high, the numerical results become closer to the volume-energy formula. Deviation in the lower velocity range is reasonable because the elastic and plastic deformation plays an important role, and the craters cannot be created until the velocity increases to a threshold value. When the velocity is high, the magnitude of the stress wave is much larger than the strength of the projectile and the target. The material deforms like fluid in high-velocity range, where the volume-energy formula is applicable and MPM results agree well.

### 3.4. MPM results of oblique high-velocity impact

The process of oblique impact with  $v_p = 2200$  m/s and inclined angle  $30^\circ$  is shown in Fig. 8. Symbols and contour legend same as those in Fig. 5 are adopted. Fig. 8(a)–(d) show the stress contour, and Fig. 8(e)–(h) show the pressure contour. Different with the normal impact, the crater in oblique impact shows obvious inclination in the scraping direction. Also, most of the fragmented materials splash in the scraping direction.

The crater dimensions, including  $C_p$ ,  $D_{max}$  and  $D_{min}$ , increase when the impact velocity increases, as shown in Fig. 9. Lines with solid squares are the numerical results of crater depth, and dashed lines with upper triangles and lower triangles represent the lengths of the major axis and the minor axis, respectively. Larger

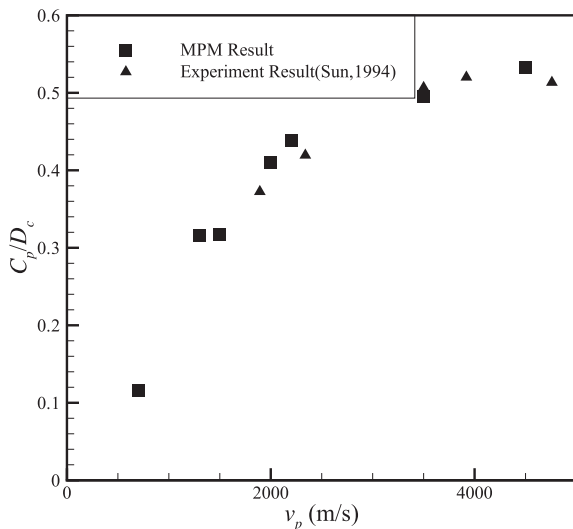


Fig. 6. Variation of the crater shape factor versus the impact velocity. Solid squares are MPM results, and solid triangles are experimental results [40].

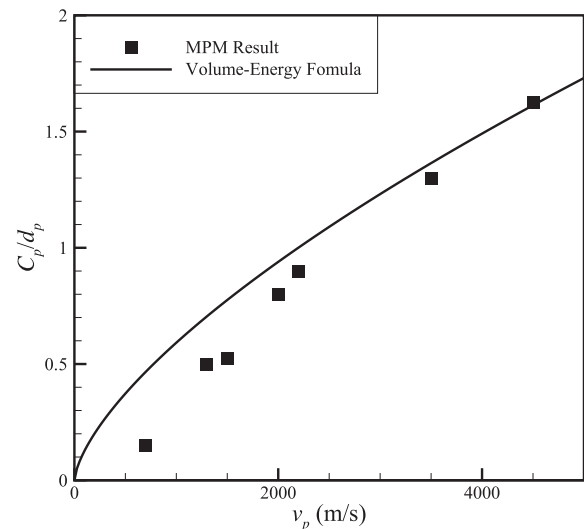


Fig. 7. Variation of the dimensionless crater depth versus the impact velocity. Solid line represents volume-energy formula, and solid squares are MPM results.

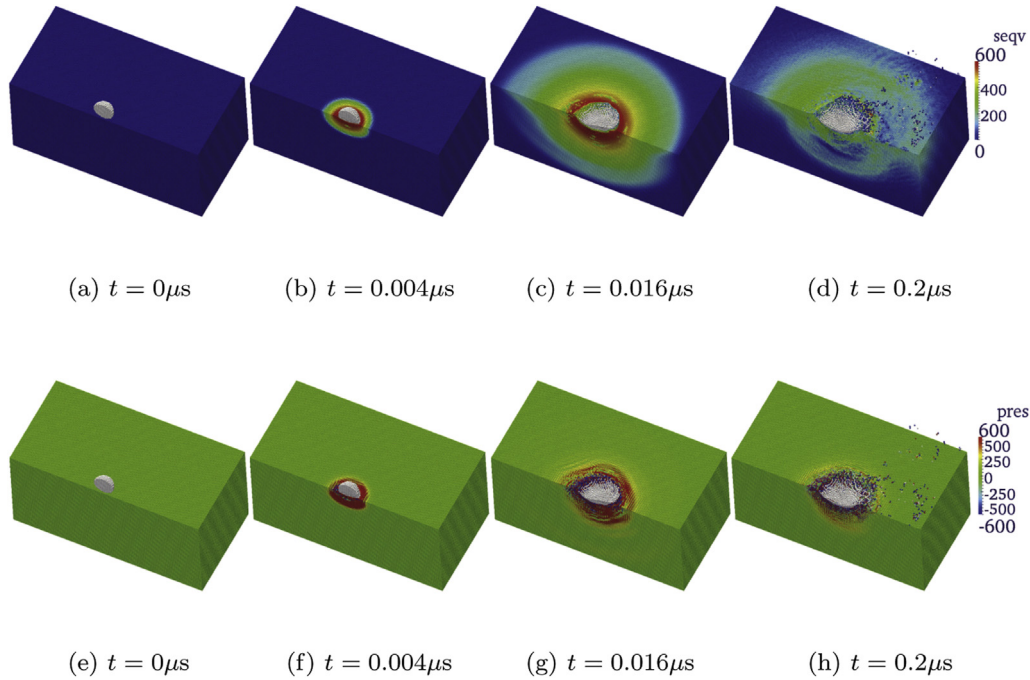


Fig. 8. Typical process of oblique impact of single particle. The impact velocity is 2200 m/s, and the inclined angle is 30°.

angle leads to smaller crater depth and larger major axis length because less energy is used to excavate the crater. But the minor axis lengths are nearly the same for inclined angles 15° and 30°.

It is important to compare the position of the crater bottom center  $C_{xb}$  and the position of the pithead center  $C_{xs}$  to determine the crater shape.  $C_{xb}$  and  $C_{xs}$  are measured in the scraping direction because the positions perpendicular to the scraping direction should be the same because of symmetry. The two positions are compared in Fig. 10, and very close results can be observed.

The eccentricity ratio  $e_1$  is defined as.

$$e_1 = \frac{2(C_{xs} - C_{xb})}{D_{max}} \quad (23)$$

which represents the deviation between the bottom center and the pithead ellipse center.  $e_1 > 0$  implies that the crater bottom center is ahead of the pithead ellipse center in the scraping direction.  $e_1 < 0$

implies that the crater bottom center is behind. Fig. 11 shows that  $e_1$  just fluctuates around zero, so the crater shape can be analyzed as an semi-ellipsoid.

The eccentricity ratio  $e_2$  of the pithead ellipse is defined as.

$$e_2 = \sqrt{1 - \left(\frac{D_{min}}{D_{max}}\right)^2} \quad (24)$$

which measures the ellipticity. The pithead shape approaches a circle when  $e_2$  approaches zero. Fig. 11 shows that when impact velocity increases,  $e_2$  increases at first and then falls. Larger inclined angle causes larger  $e_2$ , which is owing to the larger proportion of scraping energy.

Fig. 12 gives the variation of the crater shape size factors  $C_p/D_{max}$  and  $C_p/D_{min}$  at different impact angles and velocities. It is noted that

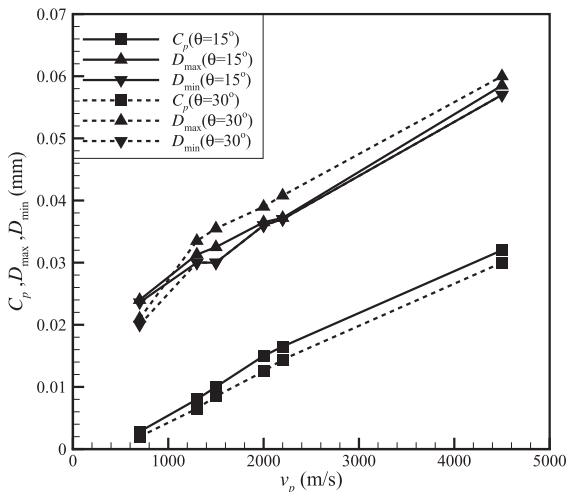


Fig. 9. The depth  $C_p$ , the major axis length  $D_{max}$  and the minor axis length  $D_{min}$  of the crater in oblique high-velocity impact at different impact angles and velocities.

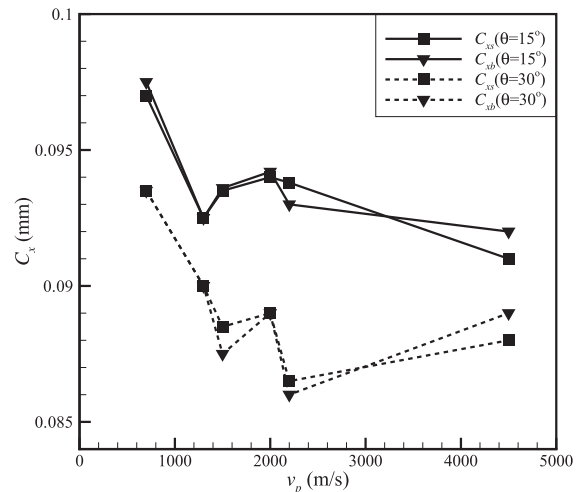


Fig. 10. The positions of the crater bottom center (lines with solid triangles) and the pithead center (lines with solid squares).

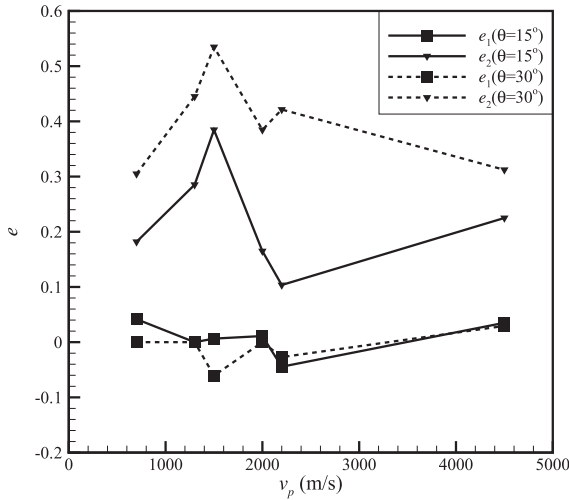


Fig. 11. The variation of eccentricity ratio  $e_1$  (lines with solid squares) and  $e_2$  (lines with solid triangles) with respect to impact velocity.

the shape factors increase rapidly at low velocities and approaches around 1/2 at high velocities, which means that the crater also approaches a hemisphere at high impact velocity. Larger inclined angle is found to cause smaller shape factors.

#### 4. High-velocity impact of particle group

##### 4.1. Problem setup

In order to simulate the LEO environment more closely, simulations of high-velocity impact of particle group are carried out to investigate the effect of impact angle, mass flux density and impact velocity on the final crater morphology.

16 spheres are used in the computational model as shown in Fig. 13. Symmetry about the scraping direction is invoked to reduce the computational cost, so that 8 craters will be created during impact.  $v_p$  is the impact velocity,  $\theta$  is the inclined angle, and  $v_n$  and  $v_s$  are the normal and the tangential velocity components.

Three slices are used to show and investigate the morphologies of the craters under different impact velocities and angles. The

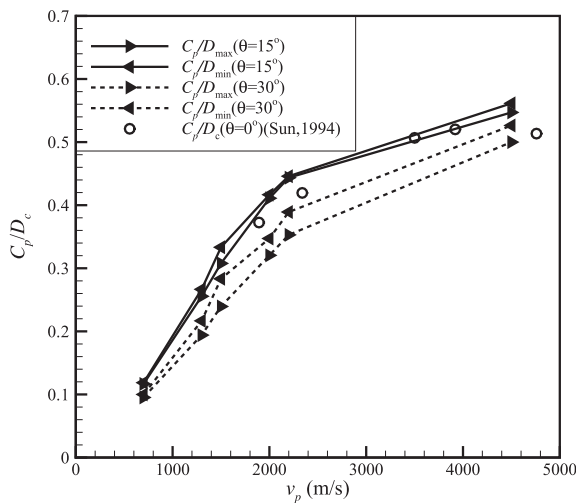


Fig. 12. The crater shape factors at different velocities and angles. Lines with solid triangles are MPM results, and hollow circles are the experimental results of normal impact [40].

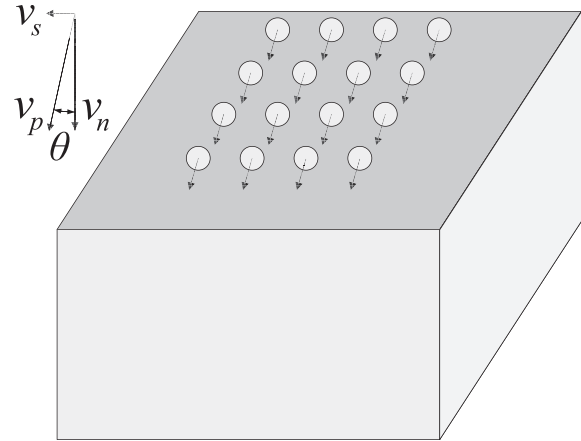


Fig. 13. Schematic diagram of high-velocity impact of particle group.

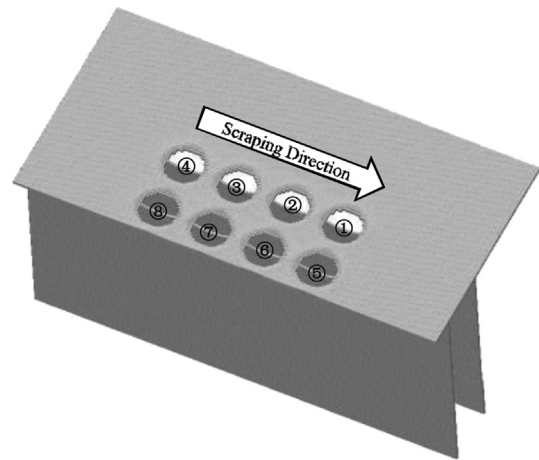


Fig. 14. Schematic diagram of the positions of three slices for analyzing crater morphologies. The numbers 1 to 8 represent different craters created by different particles.

positions and the directions of these slices to describe crater morphology and the crater numbers are shown in Fig. 14.

Three different flux densities  $\rho_f$ , including  $0.1 \text{ mg/cm}^2$ ,  $0.5 \text{ mg/cm}^2$ , and  $1.0 \text{ mg/cm}^2$ , are considered. The impact velocity  $v_p$  ranges from  $700 \text{ m/s}$  to  $4500 \text{ m/s}$  including  $700 \text{ m/s}$ ,  $1300 \text{ m/s}$ ,  $2000 \text{ m/s}$ ,  $2200 \text{ m/s}$  and  $4500 \text{ m/s}$ . The normal impact and the oblique impact of  $15^\circ$  and  $30^\circ$  are studied. The particle centers are initially located  $0.0125 \text{ mm}$  above the surface of the target in all the cases.

The convergence analysis is also carried out for the impact of particle group. Similar to the analysis for the impact of single particle, four models with different discretization scale are simulated, and their details are listed in Table 3. The variables have the same meaning as those in Table 2. The flux density is  $1.0 \text{ mg/cm}^2$ , and the impact velocity is  $4500 \text{ m/s}$ . The convergence for the dimensionless residual internal energy  $E_i^r$  and the crater depth  $C_p$  can be observed.

Table 3  
Model details and results for convergence analysis of impact of particle group.

Model no.	$h_p^t(\text{mm})$	$h_p^b(\text{mm})$	$h_e(\text{mm})$	$N_p$	$N_e$	$E_i^r$	$C_p(\text{mm})$
1	0.002	0.001	0.004	267,408	47,500	0.7515	0.0225
2	0.0015	0.00075	0.003	641,965	113,900	0.6904	0.0235
3	0.001	0.0005	0.002	2,138,048	375,000	0.6688	0.0255
4	0.0005	0.0005	0.001	16,138,048	3,000,000	0.6879	0.0265

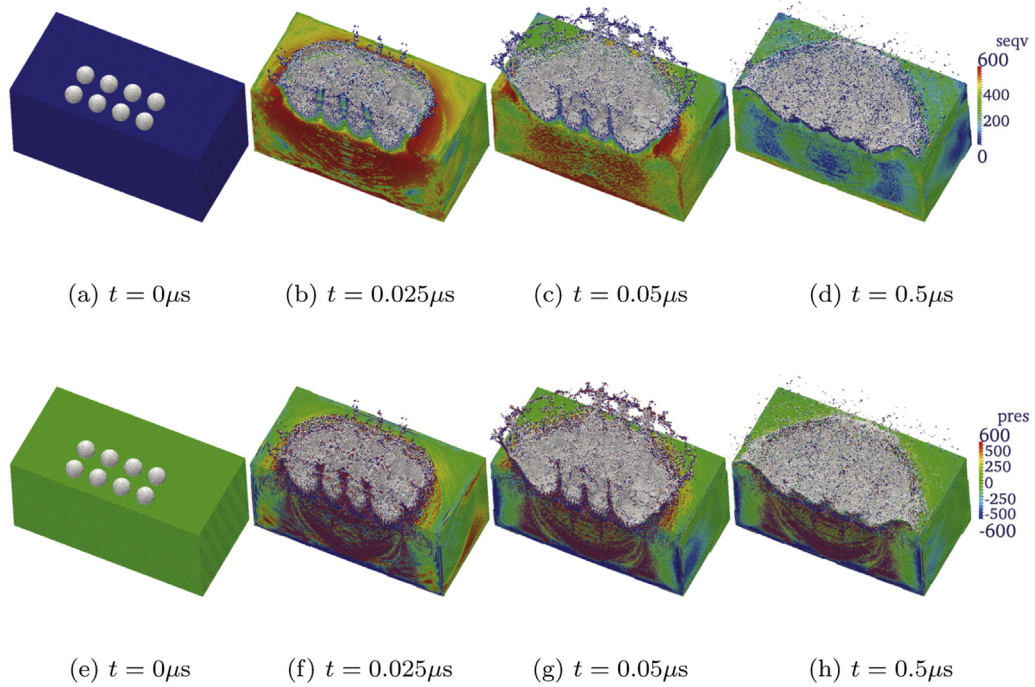


Fig. 15. Typical process of normal impact of particle group. The flux density is 1.0 mg/cm<sup>2</sup>, and the impact velocity is 4500 m/s.

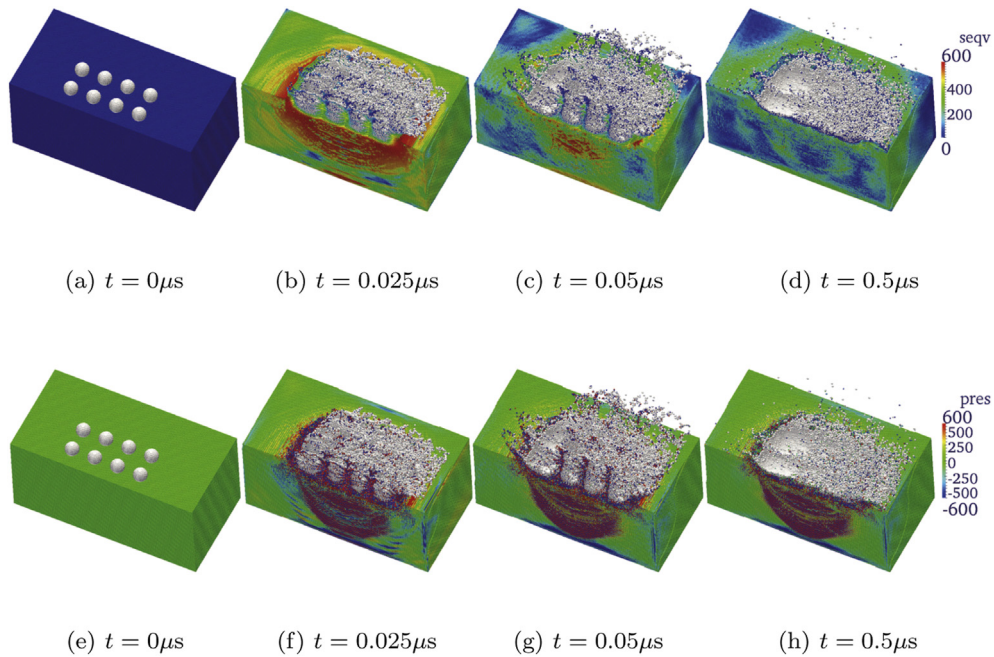


Fig. 16. Typical process of oblique impact of particle group. The flux density is 0.5 mg/cm<sup>2</sup>, the impact velocity is 4500 m/s, and the inclined angle is 30°.

The discretization model 3 (2,138,048 material points and 375,000 grid elements) is adopted for the simulation of impact of particle group.

#### 4.2. Crater morphology

A typical process of normal impact of particle group is shown in Fig. 15. The flux density is 1.0 mg/cm<sup>2</sup> and the impact velocity is 4500 m/s. The projectiles are shown with white color. The target is drawn with the effective stress contour from Fig. 15(a)–(d) and with the pressure contour from Fig. 15(e)–(h). Another process of

oblique impact is shown in Fig. 16. The flux density is 0.5 mg/cm<sup>2</sup>, the impact velocity is also 4500 m/s, and the impact angle is 30°. Stress wave propagation can be seen in the contour plots. High-level stresses are observed in the early stage of impact, but only low-level stresses exist when  $t = 0.5 \mu\text{s}$  since the shock wave has propagated into the surrounding media through the transmitting boundary and some high-level stresses are relaxed by the damage and the failure of the target material.

Crater morphologies are important in the analysis of impact results. Four modes of the crater morphology for normal impact and seven modes for oblique impact are concluded from the total

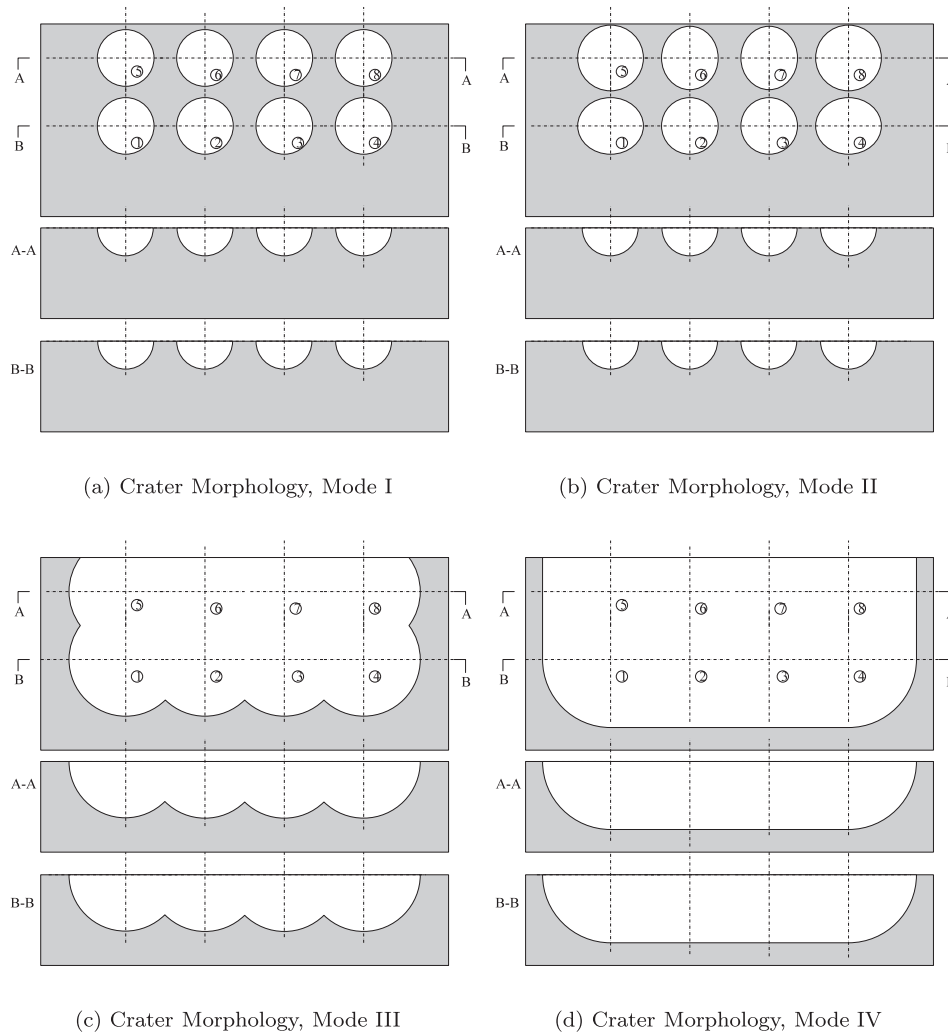


**Fig. 17.** Modes of crater morphology for normal impact. The three morphologies in each sub-figures are slices of the craters. The positions of the slices are shown in Fig. 14.

54 simulations. Fig. 17 shows the four modes for normal impact. In each sub-figure of Fig. 17, the morphologies cut by the three slices in Fig. 14 are shown from top to bottom. The top one shows the shape of crater pitheads, and the middle and the bottom ones show the side view of the crater shape. The following results can be observed.

- (I) When the impact energy is low, craters do not interact with each other, and individual crater morphology is nearly the same as that of single sphere impact, as shown in Fig. 17a.
- (II) Craters can influence each other if the impact energy increases. The middle craters change to ellipsoids, but different craters do not join to each other. This is shown in Fig. 17b.
- (III) As shown in Fig. 17c, the pitheads of the craters begin to intersect and crater surfaces connect when the impact energy is much larger, but each crater still have independent bottoms.
- (IV) As shown in Fig. 17d, the impact of particle group creates the crater shape similar to an impact of a plate when the impact energy reaches a critical value. The morphology has smooth crater bottom.

For oblique impact of particle group, seven crater morphology modes are concluded as in Fig. 18. Similar to normal impact, craters do not affect each other under low impact energy, as shown in

Fig. 18a. The shapes of the pithead are influenced by other particles under moderate impact energy, but different craters do not link to each other, as shown in Fig. 18b–d. The craters merge into one with rising and falling bottoms under large impact energy, as shown in Fig. 18e and f. Finally the craters will become a continuous crater, as shown in Fig. 18g. Different from normal impact, the scraping energy strongly influences the shape of the pithead and make the outside craters and inside craters apparently different. To be more specific, the pithead shape is more elliptical in the scraping direction, and rounder in the reverse direction, which can be observed in Fig. 18b and c. The surfaces of the inside craters in Fig. 18c and d are not ellipse. More scraping energy also result in the same effect to the outside craters as shown in Fig. 18d. The craters are linked firstly in the scraping direction and then in the perpendicular direction, which also shows the influences of scraping.

All the above discussions about the morphology modes are theoretical predictions based on computational results, since we do not find any existing experimental data on impact of particle group. But the computational results of impact of single particle are validated in the previous section, which may ensure the reliability of numerical results of particle group. The predicted crater morphology modes are expected to be further validated with future experimental work.

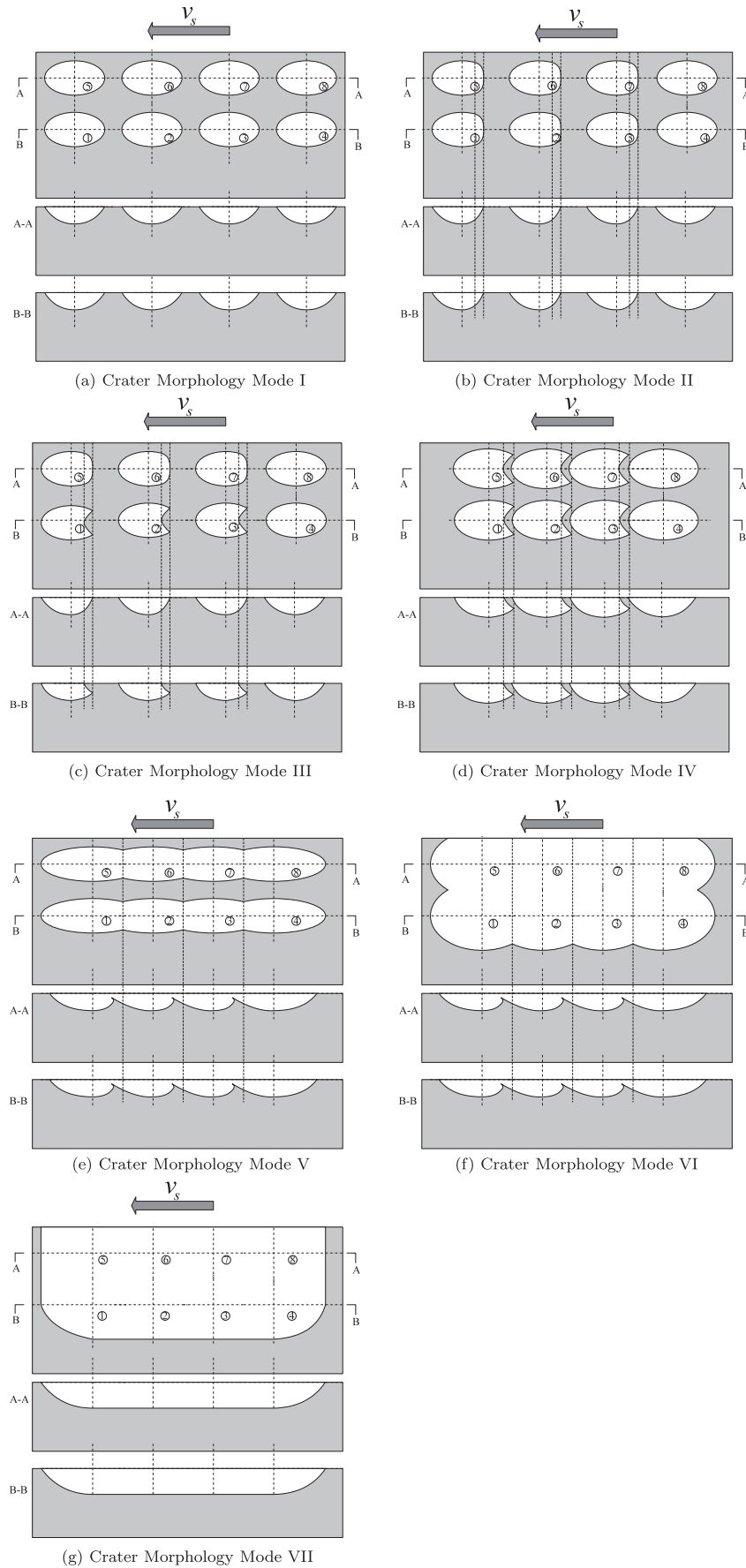


**Fig. 18.** Modes of the crater morphology for oblique impact. The three morphologies in each sub-figures are slices of the craters. The positions of the slices are shown in Fig. 14.

**Table 4**  
Classification of results of impact of particle group.

$\theta$ (°)	$\rho_f$ (mg/cm <sup>2</sup> )	700 (m/s)	1300 (m/s)	1500 (m/s)	2000 (m/s)	2200 (m/s)	4500 (m/s)
0	0.1	17a	17a	17a	17a	17a	17b
	0.5	17a	17b	17b	17b	17b	17c
	1.0	17a	17b	17b	17b	17c	17c
15	0.1	18a	18a	18b	18b	18b	18c
	0.5	18a	18b	18c	18d	18d	18f
	1.0	18b	18c	18d	18d	18e	18f
30	0.1	18a	18b	18b	18b	18b	18d
	0.5	18a	18c	18d	18d	18e	18f
	1.0	18b	18d	18d	18e	18e	18f

All computations are classified in Table 4 by these morphology modes above based on observing the simulation results. The combination of numbers and letters, such as 12a, is used to identify different modes in Table 4, where the number denotes the figure number, and the letter denotes the sub-figure number.

The impact energy flux  $E_f$  is defined as.

$$E_f = \frac{1}{2} \rho_f v_p^2 \tag{25}$$

where  $\rho_f$  is the flux density of the particle group and  $v_p$  is the magnitude of impact velocity. The normal impact energy flux  $E_f^n$  can then be defined as

$$E_f^n = \frac{1}{2} \rho_f v_n^2 = \frac{1}{2} \rho_f v_p^2 \cos^2 \theta = E_f \cos^2 \theta \tag{26}$$

where  $\theta$  is the inclined angle.

The energy flux ranges of different morphology modes are listed in Table 5. For normal impacts, the energy flux ranges have obvious bounds for different morphology modes, which means that we can determine the impact mode by the impact energy flux. Situations are more complicated in oblique impact, and the energy flux range has small overlapping. But the differences in energy flux to create different modes are still obvious. The overlapping can be understood that the transition between different modes is not abrupt but smooth. What's more, sizes of particle group and relative positions are also important factors to determine the morphology mode. Because the number of particle is fixed, the increase in energy flux implies the increase in particle size, which may have the influences on crater interactions. Generally speaking, low energy flux will create mode 18a and mode 18b; medium energy flux can cause the influences between the craters as in mode 18c and 18d; large

**Table 5**  
Energy flux ranges for different morphology modes.

$\theta$ (°)	Mode	$E_f$ (J/cm <sup>2</sup> )		$E_f^n$ (J/cm <sup>2</sup> )	
		Minimum	Maximum	Minimum	Maximum
0	17a	0.0245	0.245	0.0245	0.245
	17b	0.423	2.00	0.423	2.00
	17c	5.06	10.1	5.06	10.1
15	18a	0.0245	0.123	0.0229	0.114
	18b	0.113	0.423	0.105	0.226
	18c	0.563	1.01	0.525	0.945
	18d	1.00	2.00	0.933	1.13
	18e	2.42	2.42	2.26	2.26
	18f	5.06	10.1	4.72	9.46
30	18a	0.0245	0.123	0.0184	0.0919
	18b	0.0845	0.245	0.0634	0.184
	18c	0.424	0.424	0.317	0.317
	18d	0.563	1.13	0.422	0.844
	18e	1.21	2.42	0.908	1.82
	18f	5.06	10.1	3.80	7.59

energy flux results in linking through the craters; and much larger impact energy makes the results similar to a plate impact.

Under the same impact velocity and inclined angle the depths of different craters are close. The maximum size difference is 13%, and larger differences correspond to lower velocities. Impact velocity and inclined angle have more influences on crater depth than the position of the crater has.

### 4.3. Dimensional scaling analysis

Dimensional scaling method is typically used to obtain empirical equations from experimental results. The dimensional scaling analysis is used to obtain the relationship between the crater parameters and the model parameters. 8 parameters are considered and are categorized into three groups:

Dependent variable :  $C_p$   
 Independent variable of the projectile :  $\rho_f, \rho_p, Y_p, v_n$   
 Independent variable of the target :  $\rho_t, Y_t$

where  $C_p$  is obtained by averaging different crater depths. The crater depth is written as a function of the independent parameters,

$$C_p = F(\rho_f, \rho_p, Y_p, v_n - v_c, \rho_t, Y_t) \tag{27}$$

$v_n$  is substituted by  $v_n - v_c$  in equation (27) based on the fact that the target is excavated only when the impact velocity is beyond a threshold value.

$C_p$  can be non-dimensionalized with the sphere diameter  $d_p$ , and the other parameters are also non-dimensionalized as.

$$\frac{C_p}{d_p} = F\left(\frac{Y_t}{\rho_t(v_n - v_c)^2}, \frac{\rho_t}{\rho_p}, \frac{Y_t}{Y_p}\right) \tag{28}$$

Because the same material is used for the target and the projectile, the latter two non-dimensional scaling variables degenerate to unity.

The particle sphere diameter  $d_p$  can be calculated from the flux density.

$$d_p = \sqrt[3]{\frac{6}{\pi} \frac{ab\rho_f}{N\rho_p}} \tag{29}$$

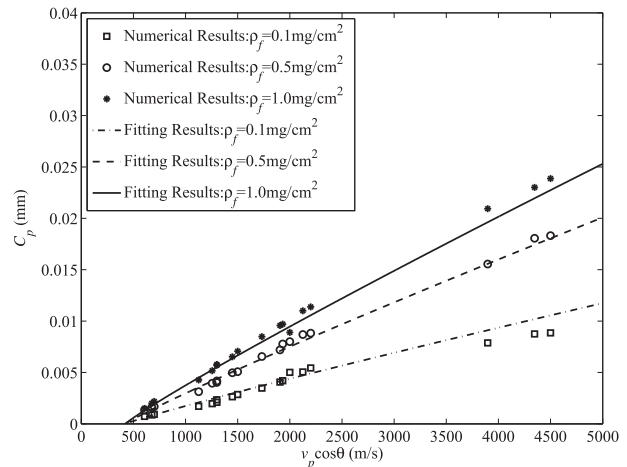


**Fig. 19.** The crater depth of MPM simulated results and the corresponding fitting curve.

where  $a$  and  $b$  are the side lengths of the rectangular region the particles initially impact, and  $N$  is the total number of particles. The normal impact velocity is expressed as

$$v_n = v_p \cos \theta \quad (30)$$

So equation (28) reduces to.

$$\frac{C_p}{\sqrt[3]{\rho_f}} \cdot \sqrt[3]{\frac{\pi N \rho_p}{6ab}} = F \left( \sqrt{\frac{\rho_t}{Y_t}} \cdot (v_p \cos \theta - v_c) \right) \quad (31)$$

A power function is assumed and fitted with the simulated results in a least-square way.

$$\frac{C_p}{\sqrt[3]{\rho_f}} \cdot \sqrt[3]{\frac{\pi N \rho_p}{6ab}} = 0.1292 \times \left[ \sqrt{\frac{\rho_t}{Y_t}} \cdot (v_p \cos \theta - 422.5) \right]^{0.9234} \quad (32)$$

The above function is in the following form for the parameters in current paper.

$$C_p = 4.896 \times 10^{-4} \rho_f^{1/3} (v_p \cos \theta - 422.5)^{0.9234} \quad (33)$$

where the unit system is mm-ms-g. Fig. 19 gives the curve of the fitted function and the numerical results. The goodness of fit is 0.9756.

## 5. Conclusion

The high-velocity impact process of single and group micron particles is investigated in detail with material point method. MPM is very efficient in solving large deformation problems, and the inherent property of ensuring non-penetration between different objects makes MPM very capable of simulating high-velocity impact problems.

The results of normal impact of single particle are compared with the experimental empirical formula. The shape factor and the depth of the crater agree well with experimental results. The oblique impacts of different inclined angles and different velocities are also investigated. Semi-ellipsoid crater is found in oblique impact, and the crater tends to a hemisphere at high impact velocity, which shows the same trends as normal impact.

The crater morphology modes are focused in impacts of particle group. Four modes for normal impact and seven modes for oblique impact are concluded based on simulated results. The crater depth is mainly influenced by the normal energy flux, and an empirical formula is proposed based on the scaling analysis. The crater shape, however, can be influenced by the scraping energy.

Future work will include the investigations on the effects of the scales of projectile. More sophisticated material models for high pressure and high temperature process should be introduced to accommodate simulations for impacts of much higher velocity.

## Funding

Supported by National Natural Science Foundation of China (Grant No. 11102097), National Basic Research Program of China (Grant No. 2010CB832701), Opening Project of State Key Laboratory of Explosion Science and Technology (Beijing Institute of Technology, Opening Project Number KFJ13-4M), and the Beijing Higher Education Young Elite Teacher Project (No. YETP0111).

## References

- [1] Drolshagen G, McDonnell JAM, Stevenson TJ, Deshpande S, Kay L, Tanner WG, et al. Optical survey of micrometeoroid and space debris impact features on EURECA. *Planet Space Sci* 1996;44(4):317–40.
- [2] Moussi A, Drolshagen G, McDonnell JAM, Mandeville J-C, Kearsley AT, Ludwig H. Hypervelocity impact on HST solar arrays and the debris and meteoroids population. *Adv Space Res* 2005;35(7):1243–53.
- [3] Zukas JA, Nicholas T, Swift HF, Greszczuk LB, Curran DR. *Impact dynamics*. New York, USA: Wiley; 1980. p. 215–40.
- [4] Mao RH, Meguid SA, Ng TY. Finite element modeling of a bird striking an engine fan blade. *J Aircr* 2007;44(2):583–96.
- [5] Beissel SR, Johnson GR. Large-deformation triangular and tetrahedral element formulations for unstructured meshes. *Comput Methods Appl Mech Eng* 2000;187(3–4):469–82.
- [6] Wang C, Zhang X, Shu C-W, Ning J. Robust high order discontinuous Galerkin schemes for two-dimensional gaseous detonations. *J Comput Phys* 2012;231(2):653–65.
- [7] Alme ML, Rhoades Jr CE. A computational study of projectile melt in impact with typical Whipple shields. *Int J Impact Eng* 1995;17(1–3):1–12.
- [8] Johnson GR, Stryk RA, Beissel SR. SPH for high velocity impact computations. *Comput Methods Appl Mech Eng* 1996;139(1–4):347–73.
- [9] Belytschko T, Lu YY, Gu L. Element-free Galerkin methods. *Int J Num Methods Eng* 1994;37:229–56.
- [10] Wang DD, Chen J-S. Locking-free stabilized conforming nodal integration for meshfree Mindlin-Reissner plate formulation. *Comput Methods Appl Mech Eng* 2004;193(12–14):1065–83.
- [11] Sulsky D, Chen Z, Schreyer HL. A particle method for history-dependent materials. *Comput Methods Appl Mech Eng* 1994;118(1–2):179–96.
- [12] Hon YC, Schaback R. On unsymmetric collocation by radial basis functions. *Appl Math Comput* 2001;119(2–3):177–86.
- [13] Zhang X, Song KZ, Lu MW, Liu X. Meshless methods based on collocation with radial basis functions. *Comput Mech* 2000;26(4):333–43.
- [14] Liu Y, Zhang X, Lu MW. A meshless method based on least-squares approach for steady- and unsteady-state heat conduction problems. *Numer Heat Transf Part B* 2005;47(3):257–75.
- [15] Johnson GR, Beissel SR, Stryk RA. A generalized particle algorithm for high velocity impact computations. *Comput Mech* 2000;25(2–3):245–56.
- [16] Huang P, Zhang X, Ma S, Huang X. Contact algorithms for the material point method in impact and penetration simulation. *Int J Numer Methods Eng* 2011;85(4):498–517.
- [17] Ma S, Zhang X, Qiu XM. Comparison study of MPM and SPH in modeling hypervelocity impact problems. *Int J Impact Eng* 2009;36:272–82.
- [18] Sulsky D, Schreyer HL. Axisymmetric form of the material point method with applications to upsetting and Taylor impact problem. *Comput Methods Appl Mech Eng* 1996;139(1–4):409–29.
- [19] Bardenhagen SG, Brackbill JU, Sulsky D. The material-point method for granular materials. *Comput Methods Appl Mech Eng* 2000;187(3–4):529–41.
- [20] Ma S, Zhang X, Lian YP, Zhou X. Simulation of high explosive explosion using adaptive material point method. *CMES Comput Model Eng Sci* 2009;39(2):101–23.
- [21] Tan HL, Nairn JA. Hierarchical, adaptive, material point method for dynamic energy release rate calculations. *Comput Methods Appl Mech Eng* 2002;191(19–20):2095–109.
- [22] Shen L. A rate-dependent damage/decohesion model for simulating glass fragmentation under impact using the material point method. *CMES Comput Model Eng Sci* 2009;49(1):23–45.
- [23] Lian YP, Zhang X, Liu Y. An adaptive finite element material point method and its application in extreme deformation problems. *Comput Methods Appl Mech Eng* 2012;241:275–85.
- [24] Liu Y, Wang HK, Zhang X. A multiscale framework for high-velocity impact process with combined material point method and molecular dynamics. *Int J Mech Mater Des* 2013;9(2):127–39.
- [25] Sulsky D, Zhou S-J, Schreyer HL. Application of a particle-in-cell method to solid mechanics. *Comput Phys Commun* 1995;87(1–2):236–52.
- [26] Ma S, Zhang X, Qiu X. Three-dimensional material point method for hypervelocity impact. *Explos Shock Waves* 2006;26(3):273–8.
- [27] Huang P, Zhang X, Ma S, Wang HK. Shared memory OpenMP parallelization of explicit MPM and its application to hypervelocity impact. *CMES Comput Model Eng Sci* 2008;38(2):119–47.
- [28] Gong W, Liu Y, Zhang X, Ma H. Numerical investigation on dynamical response of aluminum foam subject to hypervelocity impact with material point method. *CMES Comput Model Eng Sci* 2012;83(5):527–45.
- [29] Bardenhagen SG. Energy conservation error in the material point method for solid mechanics. *J Comput Phys* 2002;180(1):383–403.
- [30] Cohen M, Jennings PC. Silent boundary methods for transient analysis. In: Belytschko T, Hughes TJR, editors. *Computational methods for transient analysis*. New York: Elsevier Science Publishers B.V.; 1983. p. 301–60. Ch. 7.
- [31] Shen L, Chen Z. A silent boundary scheme with the material point method for dynamic analyses. *CMES Comput Model Eng Sci* 2005;7(3):305–20.
- [32] Johnson GR, Cook WH. A constitutive model and data for metals subjected to large strains, high strain rates and high temperatures. In: *Proceedings of the 7th international symposium on ballistics*, vol. 21; 1983. p. 541–7.
- [33] Johnson GR, Cook WH. Fracture characteristics of three metals subjected to various strains, strain rates, temperatures and pressures. *Eng Fract Mech* 1985;21(1):31–48.
- [34] Lee R, Osher J, Chau H, Gerassimenko M, Pomykal G, Speer R. The impact of flat, thin plates on aluminum targets in the 5–10 km/s velocity range. *Int J Impact Eng* 1993;14(1–4):451–65.

- [35] Wingate CA, Stellingwerf RF, Davidson RF, Burkett MW. Models of high-velocity impact phenomena. *Int J Impact Eng* 1993;14(1–4):819–30.
- [36] Meyers MA. *Dynamic behavior of materials*. New York, USA: Wiley; 1994. p. 124–51.
- [37] Herrmann W, Jones AH. Correlation of hypervelocity impact data. In: *Proceedings of the fifth symposium on hypervelocity impact*, vol. 1; 1962. p. 389–438.
- [38] Herrmann W, Wilbeck JS. Review of hypervelocity penetration theories. *Int J Impact Eng* 1987;5(1–4):307–22.
- [39] Yu S, Sun G, Tan Q. Experimental laws of cratering for hypervelocity impacts of spherical projectiles into thick target. *Int J Impact Eng* 1994;15(1):67–77.
- [40] Sun G, Tan Q, Zao C, Ge X. Cratering experiments with hypervelocity impact upon thick metallic targets. *Acta Armamentarii* 1994;1:27–31.